

Photovoltaic and dielectric properties of Bi₂S₃ thin films deposited by spray pyrolysis technique

Z. AMARA, M. KHADRAOUI*, R. MILOUA, M. N. AMROUN, K. SAHRAOUI

Laboratoire d'Elaboration et de Caractérisation des Matériaux LECM, département d'électronique, University of Djillali Liabes, BP89, Sidi Bel Abbés 22000, Algeria

Bismuth sulfide Bi₂S₃ thin films were deposited by Spray Pyrolysis method at 260°C. X-Ray Diffraction has been used to investigate the crystalline structure and the crystallite size of Bi₂S₃ thin films. The optical band gap has been determined by UV-VIS-NIR spectrophotometry. Using the measured absorption coefficient data, we estimated the expected absorption capacity and photocurrent of the thin films. The deposited thin films yield a maximum photocurrent of 33.6 mA/cm². Hall-effect measurements showed that Bi₂S₃ thin films have a lower value of resistivity of $2.82 \times 10^{-2} \Omega \text{ cm}$. This value is optimal for the improvement of solar cells based Bi₂S₃ thin films. AC conductivity obeys to the relation $A\omega^S$. The decrease of the exponent S with temperature reveals to understand the behavior hopping model CBH. The density of states $N(E_f)$ was in order of $10^{18} \text{ eV}^{-1} \text{ cm}^{-3}$.

(Received January 9, 2019; accepted April 9, 2020)

Keywords: Bi₂S₃, Thin films, Dielectric properties, Spray pyrolysis

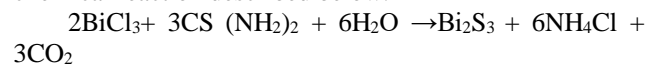
1. Introduction

During the last decade, chalcogenides materials have long been recognized as the chief component of solar energy devices [1-3]. Bi₂S₃ is a metal chalcogenide semiconductor has attracted much attention because it is an abundant and low toxic material and has a good sensibility [4,5]. In addition, it is a promising material which is widely used in different fields due to his optical and electronic properties. It is one such compound that belongs to V-VI group with orthorhombic structure. Furthermore, it has an optical band gap which lies between 1.1 and 1.7 eV [6, 7]. Bi₂S₃ thin films are n-type semiconductors with remarkable applications in thermoelectric and photo-electrochemical devices. It is deposited by a various techniques such as chemical bath deposition [8,9] SILAR method [10] microwave approach [11], spray pyrolysis [12,13].

In the present study, Bi₂S₃ was synthesized by spray pyrolysis method. First, these films have been investigated using X-ray diffraction data. The compositional details were analyzed using scanning electron microscopy (SEM) and energy dispersive analysis of X-ray (EDAX) analyzer. Then, the optical properties were investigated from reflectance and transmittance measurements. Furthermore, photovoltaic property of the films such as the photocurrent density was calculated using the measured absorption coefficient data. To explain the mechanism process and the type of polarization in these materials, the AC conductivity and the dielectric properties are investigating for different temperatures. The behavior of this latter is described from correlated barrier hopping (CBH) model [14].

2. Experimental

Bi₂S₃ thin films were obtained by dissolving BiCl₃ and thiourea (CH₄N₂S) with concentration of 0.1 M in 100 mL of bidistilled water and methanol. These solutions were mixed in 2:3 volumetric proportions. Fig. 1 presents the diagram of spray pyrolysis technique. As can be seen, the prepared solution was atomized and sprayed on the top. The spraying solution was connected to an air compressor of 6 N/cm². The glass substrates were preheated by the hot plate. When the substrates temperature is too high, there is a possibility for evaporating the sulfur. Therefore, this temperature was optimized at 260 °C and controlled by a thermocouple. It can be reduced when the solution was sprayed. Several seconds were required to recover the pre-set temperature after each step with a time interval of 2 min. After the deposition process, the obtained thin films were cooled slowly to room temperature. They were observed as grey in color. The formation of Bi₂S₃ thin films follows the chemical reaction described below:



Structural characterization has been carried out at room temperature using using a Bruker X-ray diffractometer model D2 Phaser with CuK α radiation ($\lambda = 1.5406 \text{ \AA}$). Morphology was carried out by a JEOL-JSM 5800 scanning electron. The optical transmittance and reflectance were recorded from 200 to 2500 nm wavelength using an UV (Ultra-Violet) -Visible-NIR JASCO type V-570 double beam spectrophotometer. Electrical measurements were carried out by Hall Effect using ECOPIA H MS-5000 system at room temperature.

Electrical contacts were made to each of four corners with silver paste. The dielectric and AC conduction measurements were carried out on the Bi_2S_3 sample using an impedance meter of the type HP 4192 operating in the frequency range of 5 Hz-13 MHz for different temperatures (300K-400K).

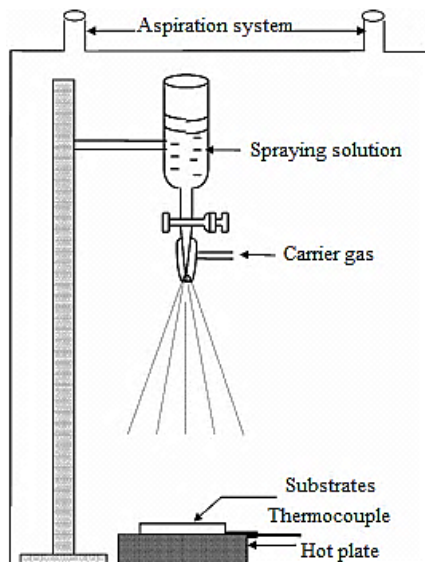


Fig. 1. Schematic diagram of spray pyrolysis technique

3. Results and discussion

3.1. Structural and morphological characterizations

The x-ray diffraction patterns of Bi_2S_3 films are shown in Fig. 2.

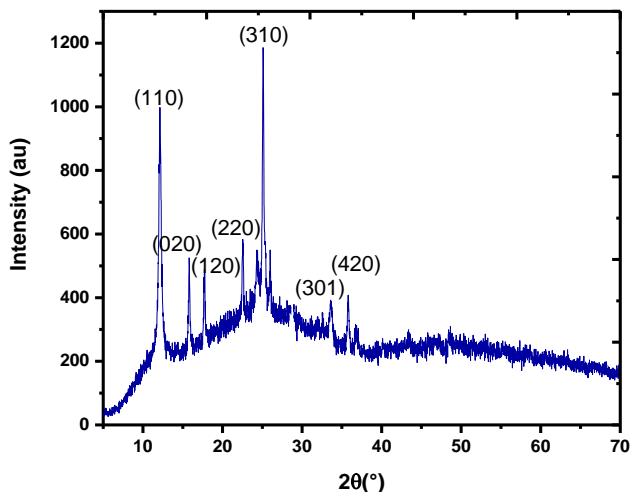


Fig. 2. Experimental X-ray diffraction pattern of Bi_2S_3 thin films

These films have not been treated after deposition. The peaks of XRD pattern have been assigned according to the JCPDS references Bi_2S_3 (card N° 17-0320). The presence of multiple diffraction peaks indicates the

polycrystalline nature of the films. The XRD patterns of the as deposited films reveal the presence of orthorhombic phase Bi_2S_3 . All the peaks are attributed to the phase of Bi_2S_3 with the dominant peak (310) reflection. Moreover, the absence of any other peaks corresponding to impurities reveals the good quality of the deposited layers. The whole peaks can be indexed to the phase of Bi_2S_3 with lattice constants $a = 11.143 \text{ \AA}$, $b = 11.17 \text{ \AA}$ and $c = 3.98 \text{ \AA}$.

In order to estimate the crystallite size and microstrain, we are used the method provided by Williamson-Hall (W-H) which takes into consideration the limited crystallite sizes of crystals and the presence of crystallographic distortions lead to Lorentzian distributions [15,16].

Fig. 3 represents W-H plot for $(\beta \cos \theta / \lambda)$ versus $(4 \sin \theta / \lambda)$. The linear fit of W-H plot gives a straight line with y-intercept equal to the inverse of the average crystallite size ($D_{\text{W-H}} = 27.7 \text{ nm}$) and the slope estimates the average value of microstrain ($\epsilon_{\text{W-H}} = -6.33 \cdot 10^{-3}$).

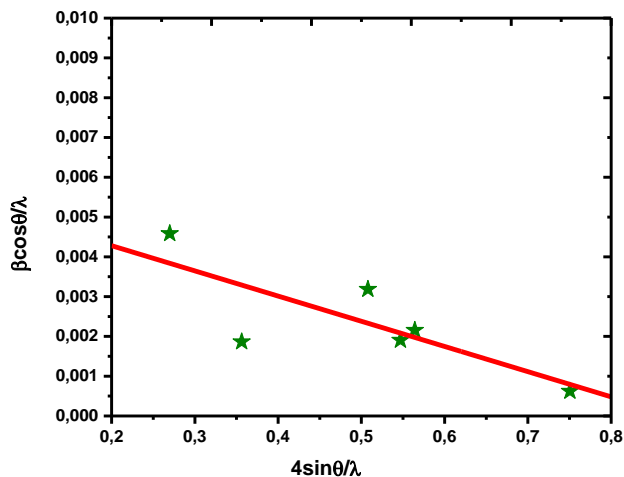


Fig. 3. Williamson-Hall plots of Bi_2S_3 thin films (color online)

In addition, Fig. 4 depicts SEM images of Bi_2S_3 thin film deposited on glass substrate. It is clear that the film obtained is dense and homogeneous in surface morphology and coats the totality of glass substrate.

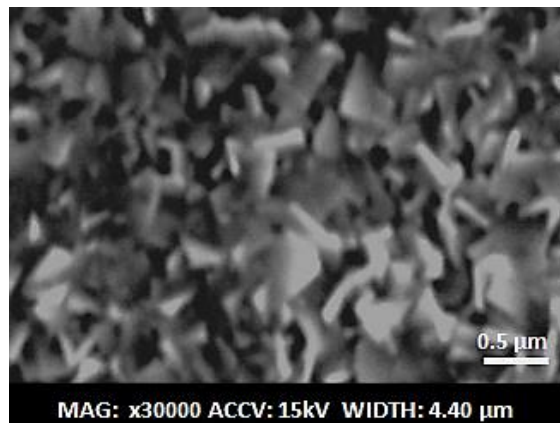


Fig. 4. SEM image of Bi_2S_3 thin film

3.2. Optical properties of Bi₂S₃

The inter-band absorption theory shows that the absorption coefficient near the threshold versus the energy obeys the following relation [17]:

$$(\alpha h\nu) = A_n (h\nu - E_g)^n \quad (1)$$

where A_n is the probability parameter for the transition and E_g the optical gap energy. For allowed direct transitions the coefficient n is equal to $\frac{1}{2}$ and for indirect allowed transitions $n = 2$. The plot of the absorption coefficient and the variation of $(\alpha h\nu)^2$ versus energy are shown in Fig. 5. The nature of the plot indicates the existence of direct transitions. The bandgap E_g is determined by extrapolation of the straight portion of the plot to the energy axis. The values (E_g) corresponding to the direct band-gap transition of the Bi₂S₃ was equal to 1.7 eV. The absorption coefficient is in the range of 10^5 cm^{-1} .

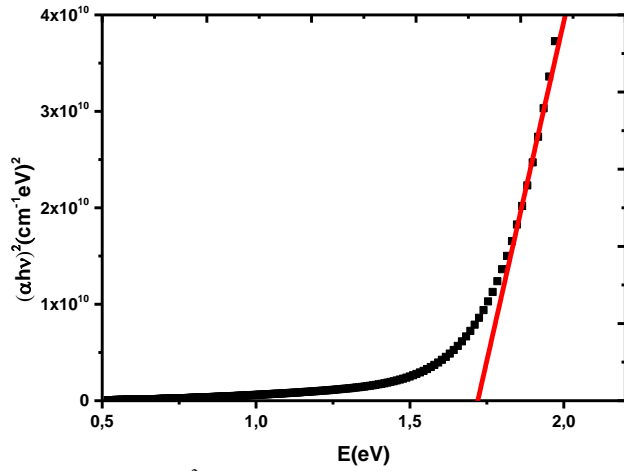


Fig. 5. $(\alpha h\nu)^2$ versus energy of Bi₂S₃ thin films (color online)

Using the measured absorption coefficient $\alpha(\lambda)$ and the refractive index values, we are estimated the expected the absorption $A(d, \lambda)$ and the photocurrent density $J_{ph}(d)$ of the films. We assumed Bi₂S₃ based solar cell with three different configurations: (a) single pass absorption when the light traverses the films only once, supposing a perfect antireflection and normal incidence; (b) double pass supposing an oblique incidence and perfect reflective back-surface, and (c) the Yablonoitch limit. This latter represents the maximum of light absorbed by films with fewer optical losses and evaluates the efficiency of light trapping. The single pass, double pass and Yablonoitch limit are calculated by Esq. 2 and 3:

For the single pass and double pass [18]

$$A(d, \lambda) = 1 - e^{-\alpha d} \quad (2)$$

Yablonoitch limit:

$$A(d, \lambda)_{\text{Yablonoitch}} = 1 - \frac{1}{1 + \alpha d 4n^2} \quad (3)$$

where p is constant represents 1 and 2 for the single pass and double pass respectively, d : is the film thickness; n : is the refractive index.

The thickness-dependent absorbed photon fraction and the photocurrent are calculated by the following relations [19]:

$$\text{Absorbed photon fraction} = \frac{\int_{300 \text{ nm}}^{\lambda_g} F(\lambda) A(d) d\lambda}{\int_{300 \text{ nm}}^{\lambda_g} F(\lambda) d\lambda} \quad (4)$$

$$J_{ph}(d) = q \times \int_{300 \text{ nm}}^{\lambda_g} F(\lambda) A(d) d\lambda \quad (5)$$

where $F(\lambda)$ is the AM1.5G photon flux, q is the electron charge and the wavelength $\lambda_g = hc/E_g$.

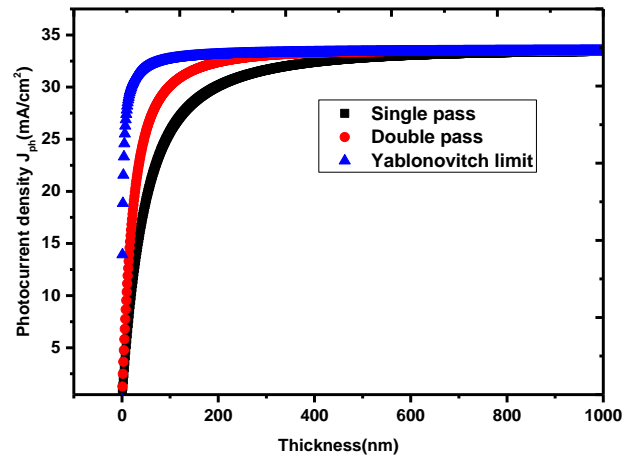


Fig. 6. Dependence of Photocurrent density with thickness (color online)

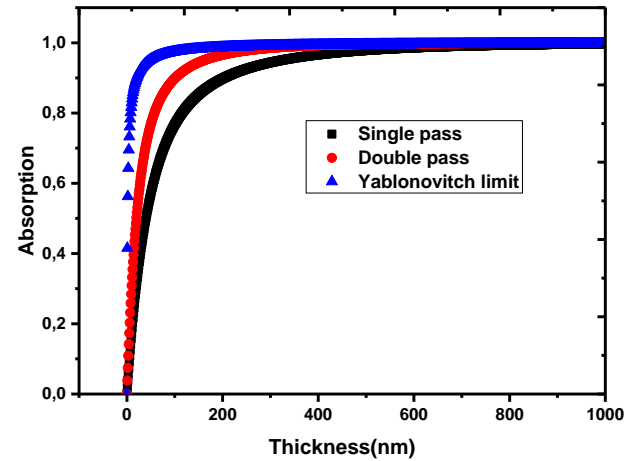


Fig. 7. Absorption spectrum versus film thickness (color online)

Fig. 6 shows the three representations of absorption versus films thickness. It can be seen that the maximum of absorption of Bi₂S₃ thin films is given by Yablonoitch limit compared with the single and the double pass absorptions. As it is shown in Fig. 7, Bi₂S₃ has a short

circuit current of 33.6 mA/cm² corresponding to Yablonovitch limit. We also notice that photocurrents are an increasing function of the thickness.

3.3. Electrical measurements

3.3.1. DC electrical measurements

In order to determine the electrical properties of Bi₂S₃ thin film such as resistivity ρ , mobility μ and carrier concentration n , we are attributed to Hall effect measurements. The results are summarized in Table 1.

Table 1. The Hall effect results of the Bi₂S₃ thin films

Resistivity ρ (Ωcm)	Bulk concentration (cm^{-3})	Mobility μ ($\text{cm}^2/\text{V.S}$)	Hall Coefficient (cm^2/C)	Free path(nm)
$2,82.10^{-2}$	$8.55.10^{19}$	2,58	$-7.2.10^{-2}$	0.2318

The negative value of Hall coefficient indicates that the films are n-type in nature. It is clear that resistivity has a lower value which implies that Bi₂S₃ is a conductor material. Therefore, the low value of mobility can be explained by the interaction between the carrier and the scattering mechanisms, such as atomic vibration, dislocation, grain boundary, ionized impurity and neutral impurity scattering. The Fermi energy level E_F was calculated using the following relation [20]:

$$E_F = \left(\frac{\hbar^2}{8m^*}\right) \left(\frac{3n}{\pi}\right)^{2/3} \quad (6)$$

where \hbar is Planck constant, $m^* = 0.2 m_e$ [21], m_e is the electron mass, n is the carrier concentration. The calculated Fermi energy E_F value (0.3642 eV) is higher than the energy corresponding to the room temperature (0.025eV), this result confirms the degeneracy of our samples. The mean free path L of the free carries is calculated through the following relation [22]:

$$L = \left(\frac{\hbar}{2e}\right) \left(\frac{3n}{\pi}\right)^{1/3} \cdot \mu \quad (7)$$

where e is the electron charge, n is the carrier concentration and μ is the mobility of charge. The result of the free path is noted in Table 1. It is considerably smaller than the crystallite size value D calculated from XRD results, which confirms that the ionized impurity and /or neutral impurity scattering are the dominant scattering mechanism in these films. This behavior is also observed by Douayar el al [23] for TCO thin films.

3.3.2. AC electrical measurements

The variation of the complex impedance spectra of Bi₂S₃ thin films at different temperatures is showed in Fig. 8.

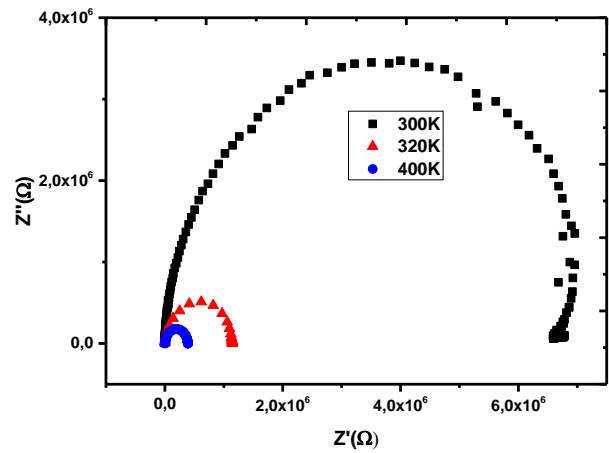


Fig. 8. Complex impedance plots at different temperatures (color online)

The experimental data obtained of these samples show that the semicircles are depressed and their centers are shifted down to the real axis indicating distribution of relaxation time ($\tau = RC$). The equivalent circuit which is modeled by Cole-Cole function is composed of resistor in parallel with capacitance [24]. The variation of the real part Z' with the imaginary part of impedance Z'' is given by [25]:

$$Z = \frac{R}{[1+(j\omega\tau)^\alpha]} = Z' - jZ'' \quad (8)$$

where ω is angular frequency and α is a parameter which characterizes the distribution of relaxation times ($0 < \alpha < 1$). The values Z' and Z'' are given by [26]:

$$Z' = \frac{R[1+(\omega\tau)^\alpha \sin\left(\frac{(1-\alpha)\pi}{2}\right)]}{[1+2(\omega\tau)^\alpha \sin\left(\frac{(1-\alpha)\pi}{2}\right) + (\omega\tau)^{2\alpha}]} \quad (9)$$

$$Z'' = \frac{R[(\omega\tau)^\alpha \cos\left(\frac{(1-\alpha)\pi}{2}\right)]}{[1+2(\omega\tau)^\alpha \sin\left(\frac{(1-\alpha)\pi}{2}\right) + (\omega\tau)^{2\alpha}]} \quad (10)$$

The capacitance value can be evaluated from the experimental semicircles using the relation $\omega RC = 1$. The bulk grain resistance (R_g) and bulk grain capacitance (C_g) values are calculated from the cole-cole plots shown in Fig. 8 by taking frequency corresponding the maximum value of Z'' . The values of R and C evaluated for all samples are tabulated in Table 2.

Table 2. Values of the resistance, capacitance at different temperatures

	300K	320K	400K
R(Ω)	$6,8.10^6$	$1,15. 10^6$	$3,9. 10^5$
C (F)	$2,1.10^{-13}$	$4,39.10^{-14}$	$1,71.10^{-13}$

It is clear that the resistor R decreases with the increase in temperature.

Fig. 9 depicts the imaginary part Z'' as function to frequency at different temperatures. The value of Z'' increases with increasing in frequency, reaching a peak

(Z''_{\max}) at (f_{\max}). Beyond this value Z'' decreases with the increase of frequency. On the other hand, the peak Z''_{\max} became weak for high values of frequency for all temperatures. This may be due to the existence of relaxation process. Moreover, the activation energy is calculated from the relaxation frequency ω_{\max} from Arrhenius law [27]:

$$\omega_{\max} = \omega_0 \exp\left(\frac{-E_a}{kT}\right) \quad (11)$$

where E_a is the activation energy, k the Boltzmann constant and T the temperature.

From Fig. 10, which represents the plot of (ω_{\max}) with $1000/T$, the activation energy is found to be 0.07 eV.

The variation of conductivity with angular frequency at different temperatures is described by the Jonscher law [25] as:

$$\sigma_t(\omega) = \sigma_{dc}(\omega) + \sigma_{ac}(\omega) = \sigma_{dc}(\omega) + A\omega^S \quad (12)$$

Fig. 11 depicts $\ln(\sigma_t)$ as function of $\ln(\omega)$. We note that in the region of low frequency, the conductivity is independent until a critical frequency, while in the high frequencies, the conductivity increases by following an exponential law. The increase in the conductivity with temperature confirms the semiconducting behavior of the prepared samples.

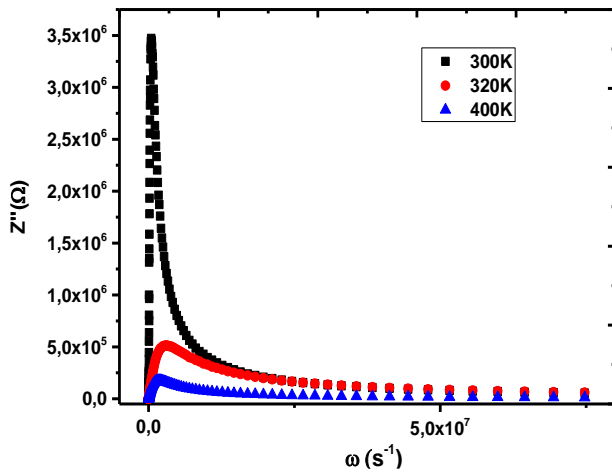


Fig. 9. The variation of the imaginary part with the angular frequency at different temperatures (color online)

From the AC conductivity (high frequency), the exponent S is calculated by the slope of its straight line.

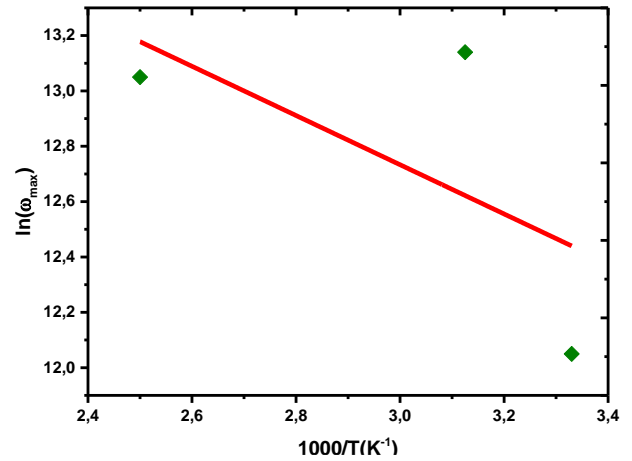


Fig. 10. $\ln(\omega_{\max})$ as function of $1000/T$ (color online)

The value of S decreases with increasing in temperature (see Fig. 12). This result leads us to understand the mechanism of conduction by CBH model which is applied in the majority of chalcogenides [28, 30]. This model is proposed to explain the electrical conductivity by thermal activation of electrons over the barrier between two sites. Each site has a coulombic potential associated with it. From the Elliot model, the exponent S is related to the temperature by the following relation [31]:

$$S = 1 - \frac{6kT}{W_m} \quad (13)$$

where w_m is the maximum of barrier.

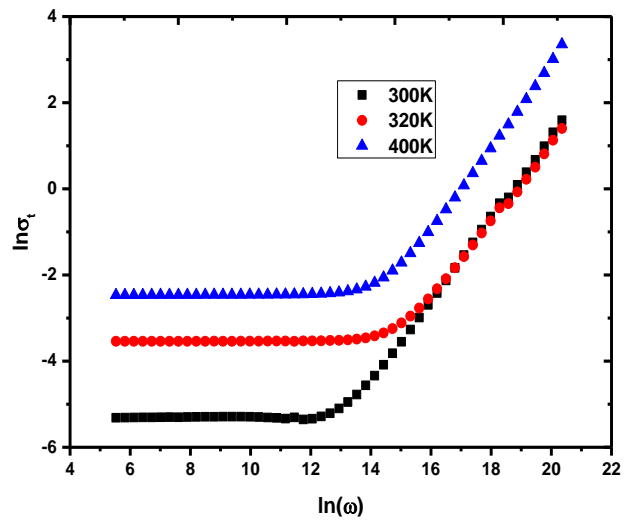


Fig. 11. Variation of $\ln(\sigma_t)$ with $\ln(\omega)$ (color online)

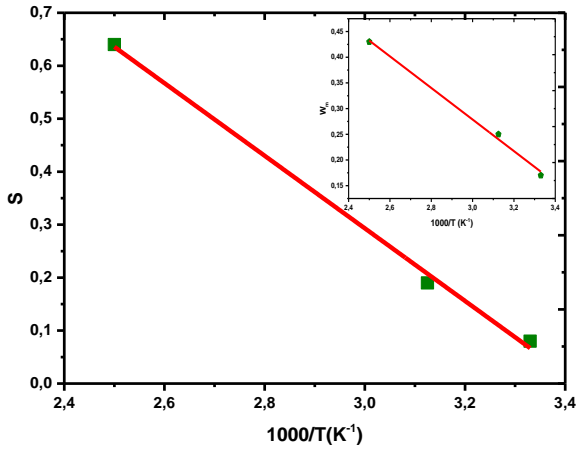


Fig. 12. The exponent S dependence of $1000/T$ (color online)

From Fig. 12, it can be seen that S was decreased with increasing in temperature and follows the same behavior of S . The maximum of barrier is often equal or less than the value of the band gap, in this study it is the quarter of the energy of band gap [32].

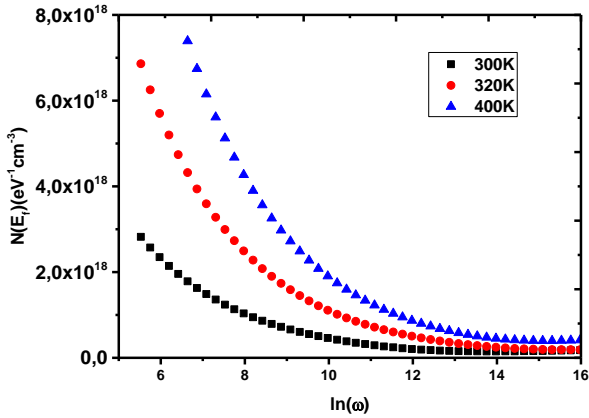


Fig. 13. The variation of the density states $N(E_f)$ with $\ln(\omega)$ at different temperatures (color online)

In CBH model, the process of hopping charges carriers in sites is associated with columbic potential; it means that it is related to the defect states pairs D^+ and D^- which formed a dipole in hopping [33]. The barrier height is correlated with the intersite separation via a Coulombic interaction

The following relation of Auttin and Mott [34,35] links the AC conductivity with the density of states $N(E_f)$ based on CBH model in order to explain jumps of electrons situated at the Fermi level [36]:

$$\sigma_{ac}(\omega) = \frac{\pi}{3} e^2 k T N(E_f)^2 \alpha^{-5} \omega \left[\text{Ln} \left(\frac{v_{ph}}{\omega} \right) \right]^4 \quad (14)$$

where e is the electronic charge, $\alpha^{-1} \sim 10 \text{ \AA}$, v_{ph} is photonic frequency $\sim 10^{12} \text{ Hz}$. The value of $N(E_f)$ is in order of $10^{18} \text{ eV}^{-1} \text{ cm}^{-3}$, which is illustrated in Fig. 13.

3.3.3. Dielectric properties

To understand the defects in solids, the study of dielectric relaxation and dielectric losses is necessary. The dielectric constant was investigated with changing in frequency and temperature; it is described by the real and the imaginary parts from the following relation [35]:

$$\varepsilon(\omega) = \varepsilon'(\omega) - j\varepsilon''(\omega) \quad (15)$$

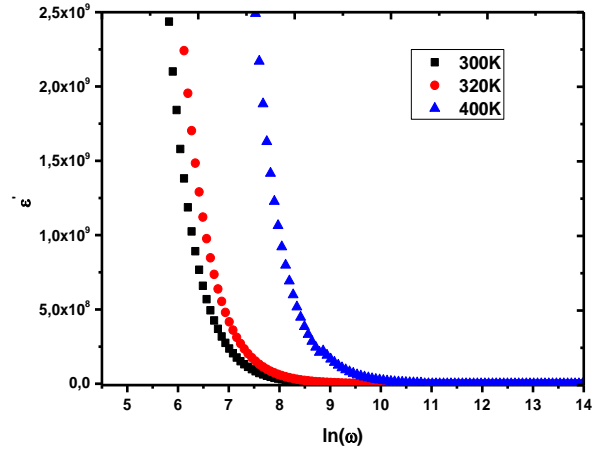


Fig. 14. $\ln(\omega)$ dependence of the dielectric constant ε' (color online)

The real and the imaginary parts $\varepsilon'(\omega)$ and $\varepsilon''(\omega)$ are calculated from the relation below [37]:

$$\sigma_{ac} = \varepsilon_0 \varepsilon'(\omega) \omega t g(\delta) \quad (16)$$

where ε_0 the permittivity of free space is, σ_{ac} is the AC conductivity, $t g(\delta)$ is the dielectric tangent loss given by:

$$t g(\delta) = \frac{\varepsilon''}{\varepsilon'} = \frac{Z_I}{Z_{II}} \quad (17)$$

The variation of $\varepsilon'(\omega)$ and $\varepsilon''(\omega)$ are illustrated in Figs. 14, 15, respectively. These parameters represent the ability to store charges and the energy loss or transfer charge. It is clear in Fig. 14 that the real part ε' decreases with increasing in frequency and approaches to a constant for all temperatures, while it increases with temperature which is observed in many works on chalcogenide glasses (semiconductors) [37, 31, 38]. Therefore, the high value of ε' at low frequency values is due to the all types of polarizability [39]. Furthermore, the dipoles in the film can follow the applied field. It may be explained by the decrease of the oriental polarizations (ions, electron, charge space..). At high value of frequency, orientational polarization decreases because it need more time to reach a steady value compared to electronic and atomic polarization. The orientation of dipoles is related to the increase in temperature and the charge carriers will excite and they contribute to the total polarization. In other words, the thermal motion of molecule is responsible of the oriental polarization and the increase in ε' . The variation of ε'' with frequency and temperature is

represented in Fig. 15. It is shown a decreasing ϵ'' with the increase of frequency and temperature. This behavior is due to the decrease of charge accumulation, the dipole cannot follow the direction of the electric field [40, 41]. At low temperature, the conduction dipole and vibrational losses are low [42]. This result leads to explain the nature of dielectric losses in the material. The dielectric losses are related to the conduction DC when ϵ'' increases with temperature [43].

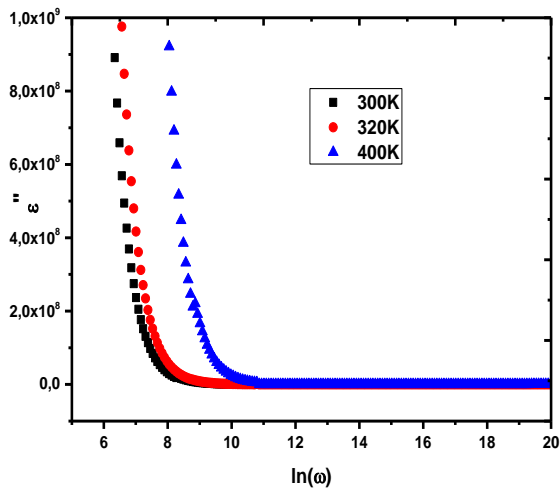


Fig. 15. $\ln(\omega)$ dependence of the dielectric loss ϵ'' (color online)

4. Conclusion

Bi₂S₃ thin films have been synthesized at 260°C by Spray pyrolysis method. Summing up the results, it can be concluded that the XRD and SEM analysis showed the presence of Bi₂S₃. For optical properties, the band gap was 1.7 eV. Using the three approximations single pass, double pass and Yablonovitch limit, it was possible to estimate theoretically the maximum absorption with perfect antireflection and normal incidence of the Bi₂S₃ thin films. The photocurrent density J_{ph} was found to be 33.6 mA/cm². The Bi₂S₃ thin films are n-type in nature. The mean free path L was observed to be lower than the grain size D calculated from XRD results which affects the mobility of carriers. The impedance study was performed in order to understand the equivalent circuit which is modeled by Cole-Cole function and the mechanism process in the structure. The AC conductivity obeys to the $A\omega^s$ law. The exponent s decreases with increasing in temperature, it led to understand the mechanism of conduction. The behavior of dielectric constant confirmed the relation between the oriental polarization and ϵ' .

Acknowledgements

The authors would like to acknowledge the financial support of this work by the General Direction of Scientific Research and Technology (DGRSDT/MESRS), Algeria,

References

- [1] Hamid S. AL-Jumaili, Mohammed Z. AL-Rawi, Y. Al-Douri, *Advanced Materials Research* **925**, 585 (2014).
- [2] Y. Al-Douri, Jamal H. Waheb, M. Ameri, R. Khenata, A. Bouhemadou, A. H. Reshak, *International Journal of Electrochemical Science* **8**, 10688 (2013).
- [3] Y. Al-Douri, M. Ameri, A. Bouhemadou, R. Khenata, *Journal of Molecular Modeling* **22**, 248 (2016).
- [4] Diego Esparzaa, Isaac Zarazúaa, Tzarara López-Lukea, Ramón Carrileza, Alejandro Torres-Castrob, Elder De la Rosa, *Electrochimica Acta* **180**, 486 (2015).
- [5] R. S. Mane, B. R. Sankapam, C. D. Lokhande, *Materials Chemistry and Physics* **60**, 196 (1999).
- [6] D. Ghanbari, M. Salavati-Niasari, S. Karimzadeh, S. Gholamrezaei, *Journal of Nanostructures* **4**(2), 227 (2014).
- [7] Geetha Govindasamy, Priya Murugasenb, Suresh Sagadevanc, *Materials Research* **20**(1), 62 (2017).
- [8] J. D. Desai, C. D. Lokhande, *Materials Chemistry and Physics* **11**, 401 (1984).
- [9] J. D. Desai, *Photoelectrochemical cells with Doped CdS Films*, Ph. D. Thesis, Shivaji University, Kolhapur, India, 1994.
- [10] Dipalu J. Desale, Shaeed Shaikh, Farha Sidoliqui, Ravikiran Birajdar, Ravikiran Cate, Anil Ghule, Ramphal Sharma, *Composites: Part B* **46**, 1 (2013).
- [11] M. Ebadi, S. Abedini, O. Rezai, M. M. Rad, *Journal of Industrial and Engineering Chemistry* **20**(5), 3821 (2014).
- [12] Z. Kebbab, N. Benramdane, M. Medles, A. Bouzidi, H. Tabet-Derraz, *Solar Energy Materials & Solar Cells* **71**, 449 (2002).
- [13] M. Medles, N. Benramdane, A. Bouzidi, A. Nekralah, H. Tabet-Derraz, Z. Kebbab, C. Mathieu, B. Khelifa, R. Desfeux, *Thin Solid Films* **497**, 58 (2006).
- [14] N. Chandel, N. Mehta, A. Kumar, *Current Applied Physics* **12**, 405 (2012).
- [15] S. J. Helen, M. Haris, T. Mahalingam, *Journal of Electronic Materials* **47**, 439 (2018)
- [16] S. Sonmezoglu, T. A. Termeli, S. Akin, I. Askeroglu, *J. Sol-Gel Sci. Technol.* **67**, 97 (2013).
- [17] J. I. Pankove, *Optical processes in semiconductors*. Englewood Cliffs, New Jersey: Prentice-Hall, (1971).
- [18] Ken Xingze Wang, Zongfu Yu, Victor Liu, Yi Cui, Shanhui Fan, *Nano. Lett.* **12**, 1616 (2012).
- [19] M. Khadraoui, R. Miloua, N. Benramdane, A. Bouzidi, K. Sahraoui, *Materials Chemistry and Physics* **169**, 40 (2016).
- [20] M. Oshima, K. Yoshino, *J. Electron Mater.* **39**, 819 (2010).
- [21] Zihang Liu, Yanling Pei, Huiyuan Geng, Jingchao Zhou, Xianfu Meng, Wei Cai, Weishu Liu, Jiehe Sui, *Nano Energy* **13**, 554 (2015).
- [22] M. Amine Fersi, I. Chaabane, M. Gargouri, *Physica E* **83**, 306 (2016).
- [23] A. Douayar, R. Diaz, F. Cherkaoui El Moursli,

- M. Abd-Lefdil, *Sensor letters* **9**, 1 (2011).
- [24] R. Dridi, I. Saafi, A. Mhamdi, A. Matri, A. Yumak, M. Haj Lakhdar, A. Amlouk K. Boubaker, M. Amlouk, *Journal of Alloys and Compounds* **634**, 179 (2015)
- [25] K. S. Cole, R. H. Cole, *J. Chem. Phys.* **9**, 342 (1941)
- [26] T. Larbi, A. Amara, L. Ben Said, B. Ouni, M. Haj, Lakhdar, M. Amlouk, *Materials Research Bulletin* **70**, 254 (2015)
- [27] M. Sassi, A. Bettaibi, A. Oueslati, K. Khirouni, M. Gargouri, *Journal of Alloys and Compounds* **649**, 642 (2015)
- [28] N. A. Hegab, A. E. Bekheet, M. A. Afifi, L. A. Wahaba, H. A. Shehata, *Journal Ovonic Research* **3**, 71 (2007).
- [29] A. M. Farid, A. E. Bekheetn, *Vacuum* **59**, 932 (2000).
- [30] A. M. Farid, H. E. Atyia, N. A. Hegab, *Vacuum* **80**, 284 (2005).
- [31] H. E. Atyia, A. M. Farid, N. A. Hegab, *Physica B* **403**, 3980 (2008).
- [32] B. Ouni, M. Haj Lakhdar, R. Boughalmi, T. Larbi, A. Boukhachem, A. Madani, K. Boubaker, M. Amlouk, *Journal of Non-Crystalline Solids* **367**, 1 (2013).
- [33] I. S. Yahia, N. A. Hegab, A. M. Shakra, A. M. AL-Ribaty, *Physica B* **407**, 2476 (2012).
- [34] I. G. Austin, N. F. Mott, *Advances in Physics* **50**, 757 (2001).
- [35] V. K. Bhatnagar, K. L. Bhatia, *Journal of Non-Crystalline Solids* **119**, 214 (1990).
- [36] R. Anuroop, B. Pradeep, *Journal of Alloys and Compounds* **702**, 402 (2017).
- [37] M. Haj Lakhdar, T. Larbi, B. Ouni, M. Amlouk, *Materials Science in Semiconductor Processing* **40**, 596 (2015).
- [38] N. Chaudhary, A. Kumar, *Indian Journal and Applied Physics* **44**, 62 (2006).
- [39] S. S. Fouad, H. E. Atyia, *Journal of Alloys and Compounds* **688**, 1206 (2016).
- [40] F. E. Salman, A. Mekki, *Journal of Non-Crystalline Solids* **357**, 1206 (2011).
- [41] A. A. Atta, *Journal of Alloys and Compounds* **480**, 564 (2009).
- [42] Saleem I. Qashou, A. A. A. Darwish, M. Rashad, Z. Khattari, *Physica B: Physics of Condensed Matter* **525**, 159 (2017)
- [43] M. M. El-Nahass, H. Kamal, M. H. Elshorbagy, K. Abdel-Hady, *Organic Electronics* **14**, 2847 (2013).

*Corresponding author: khadraoui_hm@yahoo.fr